

AFRL-RV-PS-  
TP-2012-0041

AFRL-RV-PS-  
TP-2012-0041

# **MULTI-GRID AND RESOLUTION FULL-WAVE TOMOGRAPHY AND MOMENT TENSOR INVERSION (POSTPRINT)**

## **Annual Report 2**

**Yang Shen and Wei Zhang**

**University of Rhode Island  
97 Upper College Road  
105 Wales Hall  
Kingston, RI 02881-2001**

**4 June 2012**

**Technical Paper**

**APPROVED FOR PUBLIC RELEASE; DISTRIBUTION IS UNLIMITED.**



**AIR FORCE RESEARCH LABORATORY  
Space Vehicles Directorate  
3550 Aberdeen Ave SE  
AIR FORCE MATERIEL COMMAND  
KIRTLAND AIR FORCE BASE, NM 87117-5776**

# REPORT DOCUMENTATION PAGE

Form Approved  
OMB No. 0704-0188

Public reporting burden for this collection of information is estimated to average 1 hour per response, including the time for reviewing instructions, searching existing data sources, gathering and maintaining the data needed, and completing and reviewing this collection of information. Send comments regarding this burden estimate or any other aspect of this collection of information, including suggestions for reducing this burden to Department of Defense, Washington Headquarters Services, Directorate for Information Operations and Reports (0704-0188), 1215 Jefferson Davis Highway, Suite 1204, Arlington, VA 22202-4302. Respondents should be aware that notwithstanding any other provision of law, no person shall be subject to any penalty for failing to comply with a collection of information if it does not display a currently valid OMB control number. PLEASE DO NOT RETURN YOUR FORM TO THE ABOVE ADDRESS.

1. REPORT DATE (DD-MM-YYYY) 04/06/2012		2. REPORT TYPE Technical Paper		3. DATES COVERED (From - To) 01 Sep 2010 to 19 Mar 2012	
4. TITLE AND SUBTITLE Multi-Grid and Resolution Full-Wave Tomography and Moment Tensor Inversion (Postprint)		Annual Report 2		5a. CONTRACT NUMBER FA9453-10-C-0217	
				5b. GRANT NUMBER	
				5c. PROGRAM ELEMENT NUMBER 62601F	
				5d. PROJECT NUMBER 1010	
6. AUTHOR(S) Yang Shen and Wei Zhang		5e. TASK NUMBER PPM00000915		5f. WORK UNIT NUMBER EF004084	
7. PERFORMING ORGANIZATION NAME(S) AND ADDRESS(ES) University of Rhode Island 97 Upper College Road 105 Wales Hall Kingston, RI 02881-2001				8. PERFORMING ORGANIZATION REPORT NUMBER	
9. SPONSORING / MONITORING AGENCY NAME(S) AND ADDRESS(ES) Air Force Research Laboratory Space Vehicles Directorate 3550 Aberdeen Ave SE Kirtland AFB, NM 87117-5776				10. SPONSOR/MONITOR'S ACRONYM(S) AFRL/RVBYE	
				11. SPONSOR/MONITOR'S REPORT NUMBER(S) AFRL-RV-PS-TP-2012-0041	
12. DISTRIBUTION / AVAILABILITY STATEMENT Approved for public release; distribution is unlimited. (LA-UR-11-04823).					
13. SUPPLEMENTARY NOTES Published in The Proceedings of the 2011 Monitoring Research Review – Ground-Based Nuclear Explosion Monitoring Technologies, 13 – 15 September 2011, Tucson, AZ, Volume I, pp 178-187. Government Purpose Rights.					
14. ABSTRACT There is a general consensus that 3D reference models can be used to isolate effects of wave propagation and thus help in improving characterization of seismic sources. Advances in computation and numerical method have made it possible to capture increasingly broadband, full wave generation and propagation in 3D earth models. The main objectives of this project are to construct hierarchical, multi-grid (resolution) joint P and S velocity models and the corresponding finite-difference strain Green's tensors (FDSGT) for rapid seismic moment determination. Up to 21 years continuous seismic data from broadband seismic stations in the eastern hemisphere (latitude 55S-55N; longitude 30W-157E) have been collected and processed. Empirical Green's functions derived from ambient seismic noise show clear Rayleigh waves over a broad frequency range. Over ~10,000 phase delays in 6 period bands ranging from 50 s to 600 s measured, which provide new constraints on the entire upper mantle, including the upper mantle transition zone. Several iterations of full-wave tomographic inversion have been carried out to obtain a joint P and S velocity model. Preliminary results clearly show high-velocity anomalies associated with plate subduction beneath Indonesia, southern Tibet, Iran, and the Hellenic arc. The African cratons and the west Australian craton appear as prominent high-velocity features. The eastern African Rift and Afar have deep-rooted low-velocity anomalies. Future work includes integration of earthquake arrivals and ambient noise data.					
15. SUBJECT TERMS Seismic velocity models, Ambient noise, Finite-difference strain Green's tensors					
16. SECURITY CLASSIFICATION OF:		17. LIMITATION OF ABSTRACT Unlimited	18. NUMBER OF PAGES 14	19a. NAME OF RESPONSIBLE PERSON Robert J. Raistrick	
a. REPORT Unclassified	b. ABSTRACT Unclassified			c. THIS PAGE Unclassified	19b. TELEPHONE NUMBER (include area code)

**MULTI-GRID AND RESOLUTION FULL-WAVE TOMOGRAPHY AND MOMENT TENSOR  
INVERSION**

Yang Shen and Wei Zhang

University of Rhode Island

Sponsored by the Air Force Research Laboratory

Award No. FA9453-10-C-0217

**ABSTRACT**

There is a general consensus that 3D reference models can be used to isolate effects of wave propagation and thus help in improving characterization of seismic sources. Advances in computation and numerical method have made it possible to capture increasingly broadband, full wave generation and propagation in 3D earth models. The main objectives of this project are to construct hierarchical, multi-grid (resolution) joint P and S velocity models and the corresponding finite-difference strain Green's tensors (FDSGT) for rapid seismic moment determination. In the first year of a three-year project, we collected and processed up to 21 years continuous seismic data from broadband seismic stations in the eastern hemisphere (latitude 55°S-55°N; longitude 30°W-157°E). Empirical Green's functions derived from ambient seismic noise show clear Rayleigh waves over a broad frequency range. We measured over ~10,000 phase delays in 6 period bands ranging from 50 s to 600 s, which provide new constraints on the entire upper mantle, including the upper mantle transition zone. Several iterations of full-wave tomographic inversion have been carried out to obtain a joint P and S velocity model. Preliminary results clearly show high-velocity anomalies associated with plate subduction beneath Indonesia, southern Tibet, Iran, and the Hellenic arc. The African cratons and the west Australian craton appear as prominent high-velocity features. The eastern African Rift and Afar have deep-rooted low-velocity anomalies. Future work includes integration of earthquake arrivals and ambient noise data.

## OBJECTIVES

The main objectives of this project are to construct hierarchical, multi-grid (resolution) joint P and S velocity models of the Middle East and East Eurasia and the corresponding FDSGTs for rapid earthquake/explosion moment determination.

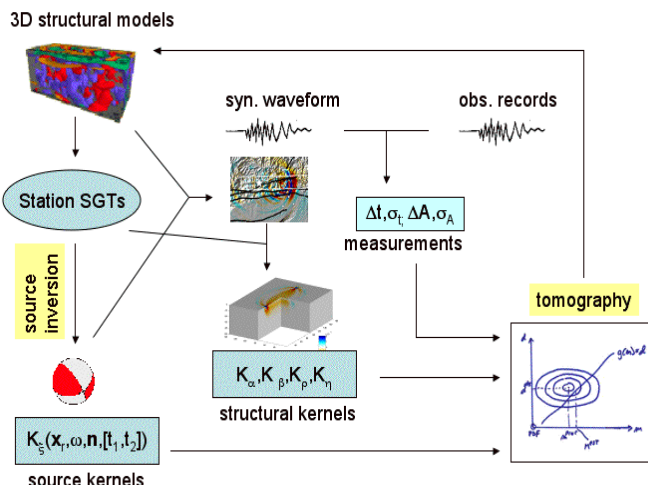
## RESEARCH ACCOMPLISHED

Much of our effort during the first year of this three-year project have been on the development of a full-wave tomographic method using ambient seismic noise and its application to obtain a joint P and S velocity model of the eastern hemisphere (latitude 55°S-55°N, longitude 30°W-157°E). In the following, we begin with a brief introduction to the project and the approach we are taking. We report the preliminary results of full-wave ambient noise tomography of the eastern hemisphere and conclude with plans for remaining work.

### Introduction

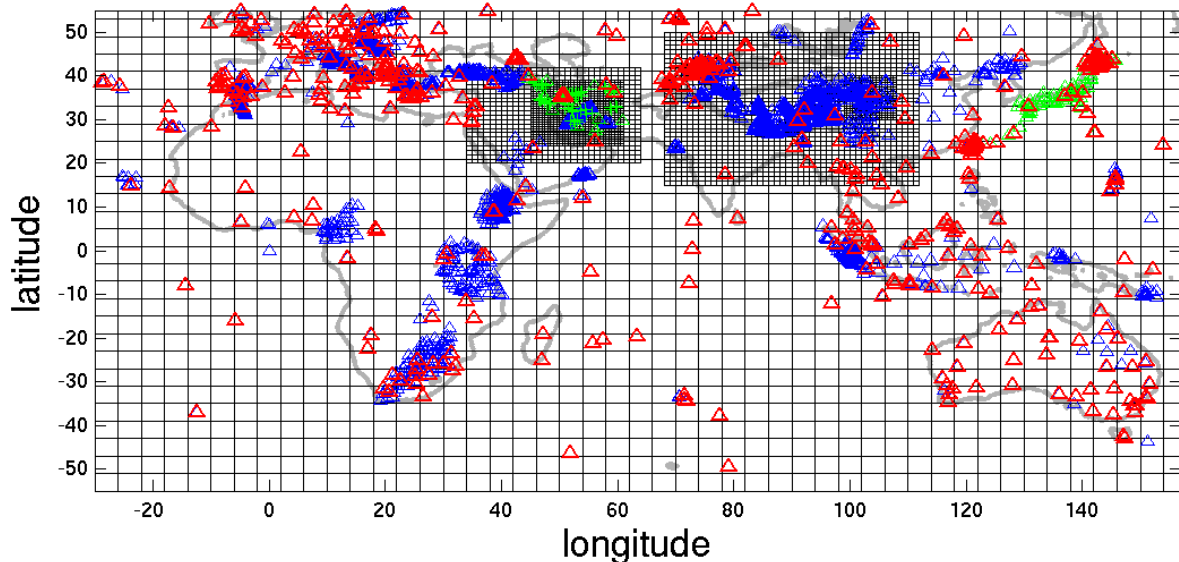
There is a general consensus that the use of 3D models improves seismic characterization (Antoun et al., 2008). Advances in computation and numerical methods have made it possible to capture increasingly broadband, full wave generation and propagation in 3D Earth models. But it is still impractical to routinely simulate forward wave propagation from the source in 3D regional models in real time. One way to overcome this computational challenge is to take advantage of an important property in seismic wave propagation, the source-receiver reciprocity. The use of the reciprocity property and Green's functions can drastically reduce computational costs when the sources outnumber the stations (e.g., Eisner and Clayton, 2001; Graves and Wald, 2001). More importantly, with 3D Green's functions pre-calculated and saved in a database, they can be extracted quickly from the database after a seismic event and used to determine seismic moments (Zhao et al., 2006; Shen et al., 2011).

Figure 1 is a schematic illustration of the unified tomography and source moment inversion based on 3D Strain Green Tensor (SGT) databases. Station SGTs are constructed from 3D reference models by finite-difference simulation of the responses to orthogonal unit impulsive point forces acting at stations. By extracting SGTs in a small volume surrounding the source reference location, we can invert for source moment tensors and location in a global optimization scheme. Travel time and amplitude anomalies are measured from the observed and synthetic waveforms at stations. The forward wave field from the source and SGTs are used to calculate finite-frequency sensitivities of the measurements to perturbations in  $V_p$ ,  $V_s$  (Zhao et al., 2005; Zhang et al., 2007; Zhang and Shen, 2008; Shen et al., 2008). Together with the sensitivities to source parameters, the measurements and sensitivity kernels are used to invert for the Earth's structure (e.g., Chen et al., 2007; Shen and Zhang, 2010). The inversion results and additional constraints (e.g., receiver function solutions) are added to the 3D model. This process can be repeated to progressively improve the solutions. For full-wave tomography using ambient noise, the source moment inversion is omitted and the synthetic waveforms at stations and sensitivity kernels are all calculated from SGTs.



**Figure 1. Flow chart of the unified tomography and moment tensor inversions based on 3D FDSGT databases.**

One of the main challenges in full-wave tomography is the intense computation associated with simulating wave propagation in 3D models. To reduce computational cost, which often scales linearly with the number of discrete nodes in numerical methods, we adapt a multigrid/multilevel method (Briggs, 1987) to solve the wave propagation and inversion problem using a hierarchy of discretization (Figure 2). We use three levels of finite-difference computational grids at the hemispherical, regional-, and local-scales to progressively construct a hierarchical, multi-resolution model. Data analysis will correspondingly evolve from long period waves for teleseismic observations to broadband waves for local and regional observations. Two areas are selected for detailed studies: (1) the Middle East, and (2) the Tibetan plateau and surrounding areas. Each focus area will have a self-consistent P and S velocity model from full-wave tomography and the FDSGT databases for seismic stations at local and teleseismic distances.



**Figure 2.** A hierarchical, multi-grid (resolution) approach to develop a joint P and S velocity model in Eurasia, Africa and Australia. The three levels of grid represent the finite-difference grids used in simulations of wave propagation in 3D models at continental, regional, and local scales. The finest grid has a grid spacing of 500-1000 m. For legibility, the grids shown have been down-sampled to approximately every 25 grids. Triangles mark the permanent (red) and temporary (blue) stations that are available or will be available during the project at the IRIS DMC. Also plotted are the broadband Japanese seismic network (F-net, green triangles), Iranian National Seismic Network (INSN, green triangles), and Iranian Seismic Telemetry Network (IRSC, green crosses).

### Full-Wave Ambient Noise Tomography of the Eastern Hemisphere

#### Reference Model and Wave Propagation Simulation

The initial 3D reference model is composed of CRUST 2.0 (Bassin et al., 2000) for the crust and AK135 (Kennett et al., 1995) for the mantle. The choice of an average Earth model for the mantle instead of one of the current 3D models (e.g., Ritsema and van Heijst, 2000; Ritzwoller et al., 2002; Antolik et al., 2003) is a tradeoff between finding a good starting model and the needs to explore a wide enough model space and validate the final solution.

We use a non-staggered grid to simulate wave propagation in a spherical coordinate (Figure 3, Zhang et al., 2011). We implement the DRP/opt MacCormack scheme, which alternately uses forward and backward finite-difference operators, in the calculation. The solution is optimized for both dispersion error and dissipation error, and has a 4th-order dispersion accuracy. In order to increase the efficiency of the finite-difference algorithm, we use a grid with non-uniform grid spacing to discretize the computational domain. The grid varies continuously with smaller spacing in low velocity layers and with larger spacing otherwise. The computational domain is surrounded by complex-frequency shifted Perfect Matched Layers (PMLs) implemented through auxiliary differential equations (Zhang and Shen, 2010).

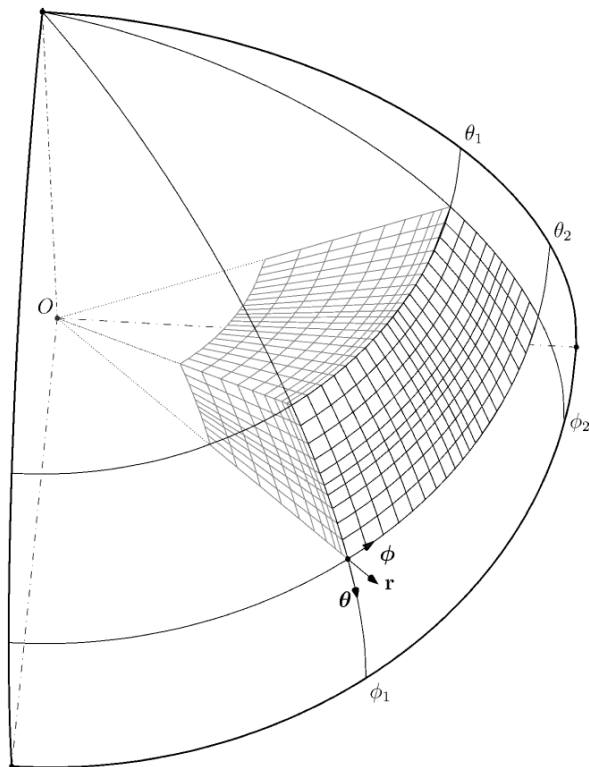


**Figure 3. Geometry of non-uniform, non-staggered finite-difference grid in a spherical coordinate system.**

The computational domain covers the eastern hemisphere (latitude 55°S-55°N; longitude 30°W-157°E) with a lateral grid spacing of 0.2°, and a non-uniform grid from the surface to ~2100 km depth (3 km near surface, and gradually increasing to ~40 km near the bottom of the model). There are 12 PMLs surrounding the model boundaries except the free surface. Figure 4 shows a snapshot of simulated seismic response to a vertical force at station BJT (Beijing).

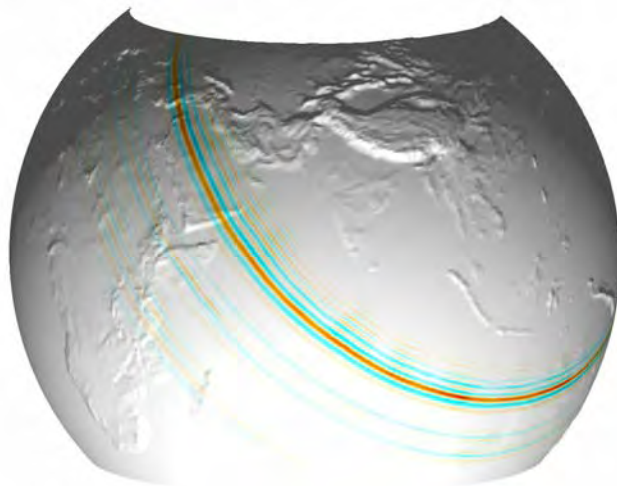


**Figure 4. A snapshot of the seismic response at the surface (vertical ground-motion velocity) to a vertical force at station BJT (Beijing).**

### Empirical Green's Functions

We collected continuous data from broadband seismic stations in the eastern hemisphere during 1990 to 2010. We selected 184 stations having at least 300 days of continuous records for further analysis. We removed instrument response from the data and normalized waveforms by the Time Frequency Normalization method (Ekström et al., 2009). We removed time windows with large ( $M_s > 5.5$ ) earthquakes. Daily records from station pairs were cross-correlated and stacked to obtain the Empirical Green's Functions (EGF). Figure 5 shows an example of EGFs from cross correlation of vertical-vertical component. Our results confirm that Rayleigh waves can be clearly extracted from seismic "hum," or earth's background free oscillation (Nishida et al., 2009). Furthermore, we extend the useful period from 400 s (Nishida et al., 2009) up to 600 s! Notice the remarkably good symmetry of very-long period ( $>100$  s) EGFs for the positive and negative time lags. These long-period waves help extend surface wave constraints to all depths of the upper mantle and uppermost lower mantle.

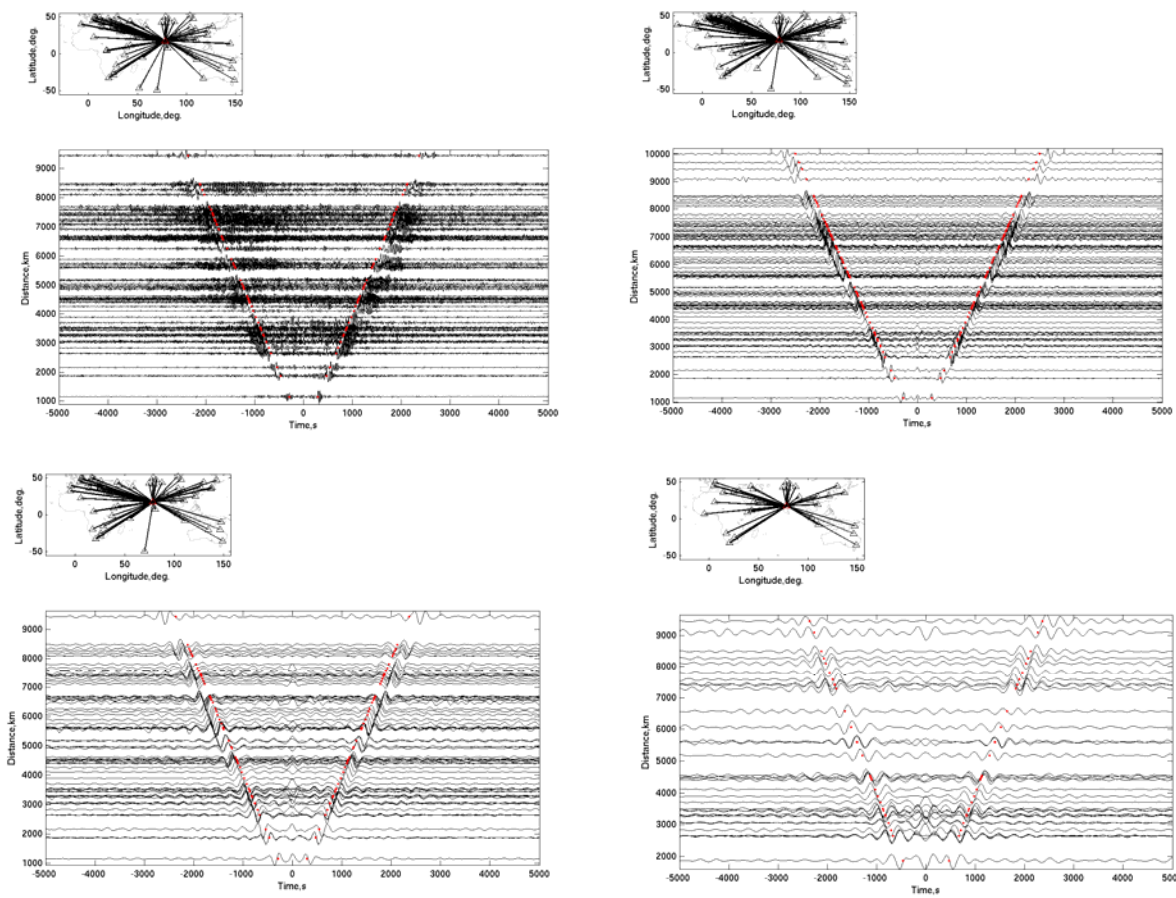


**Figure 5. Example of EGFs derived ambient noise (Earth "hum") with various wave periods (upper left: 50-600 s; upper right: 100-600 s; lower left: 200-600 s; and lower right: 300-600 s). The lines in the accompanying maps show the paths with high signal-to-noise arrivals from the virtual source (station HYB) to other receivers in the eastern hemisphere. The red dots mark a wave propagating at a velocity of 3.9 km/s.**

We measure Rayleigh wave phase delays by cross-correlating observed and synthetic Green's functions. The waveforms are band-pass filtered in six period ranges (50-100, 75-150, 100-200, 150-300, 200-400, and 300-600 s). A total of  $\sim 11,000$  phase delay measurements meet our data selection criteria (waveform correlation coefficient greater than 0.85 and signal-to-noise ratio greater than 7 for continental station pairs and 5 for those with at least one island station). Most of the propagation paths with useful waves are in the northern hemisphere (Figure 6).

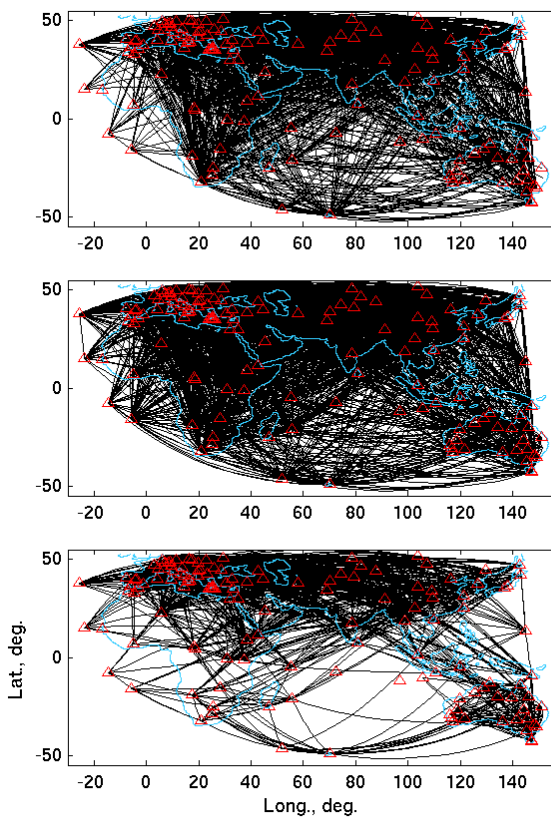


**Figure 6.** Great circle paths of useful Rayleigh wave delays from EGFs at 200-400 (top), 100-200 (middle), and 50-100 s (bottom) periods. Triangles mark the locations of seismic stations. Eurasia, northern Africa and Australia are well sampled at all periods used. The Indian and Atlantic oceans are poorly sampled, especially at relatively short (50-100 s) periods.

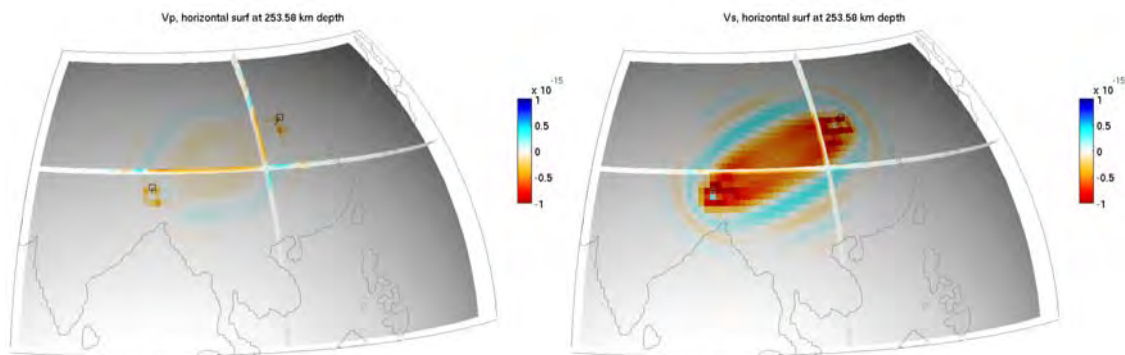


**Figure 7.** Finite-frequency sensitivity of long-period EGFs between BJT (Beijing) and LSA (Lhasa) to Vp (left) and Vs (right) perturbations. The Rayleigh wave period is 150-300 s. The horizontal slice is at ~250 km depth. Notice that the sensitivity to Vp is mostly in the upper 100 km. The unit of the sensitivity kernel is  $\text{s/m}^3$ .

#### Finite-Frequency Sensitivity Kernels

The cross-correlation of vertical-vertical component yields predominantly Rayleigh waves in the time window and frequency of our interest. Although commonly neglected in surface wave tomography, P-wave speed affects

Rayleigh waves (Figure 7). The sensitivity to P-wave speed is near the surface (the depth of sensitivity increases with period) and at a level comparable to the Vs kernel near the surface.

#### Inversion and the Preliminary Velocity Model

We represent the Rayleigh wave delays as a joint  $V_p$  and  $V_s$  inverse problem linearized relative to an iteratively updated 3D model,

$$\delta t = \int [K_\alpha(\mathbf{m}_0, x) \Delta \mathbf{m}_\alpha + K_\beta(\mathbf{m}_0, x) \Delta \mathbf{m}_\beta] dV \quad (1)$$

where  $\delta t$  is the travel time delay relative to the synthetics for the 3D model  $\mathbf{m}_0$ ,  $\Delta \mathbf{m}_\alpha$  and  $\Delta \mathbf{m}_\beta$  perturbations to P-wave and S-wave speeds, respectively,  $K_\alpha$  and  $K_\beta$  the sensitivity kernels to P-wave and S-wave speeds, respectively. The integration is for the 3D volume of the model.

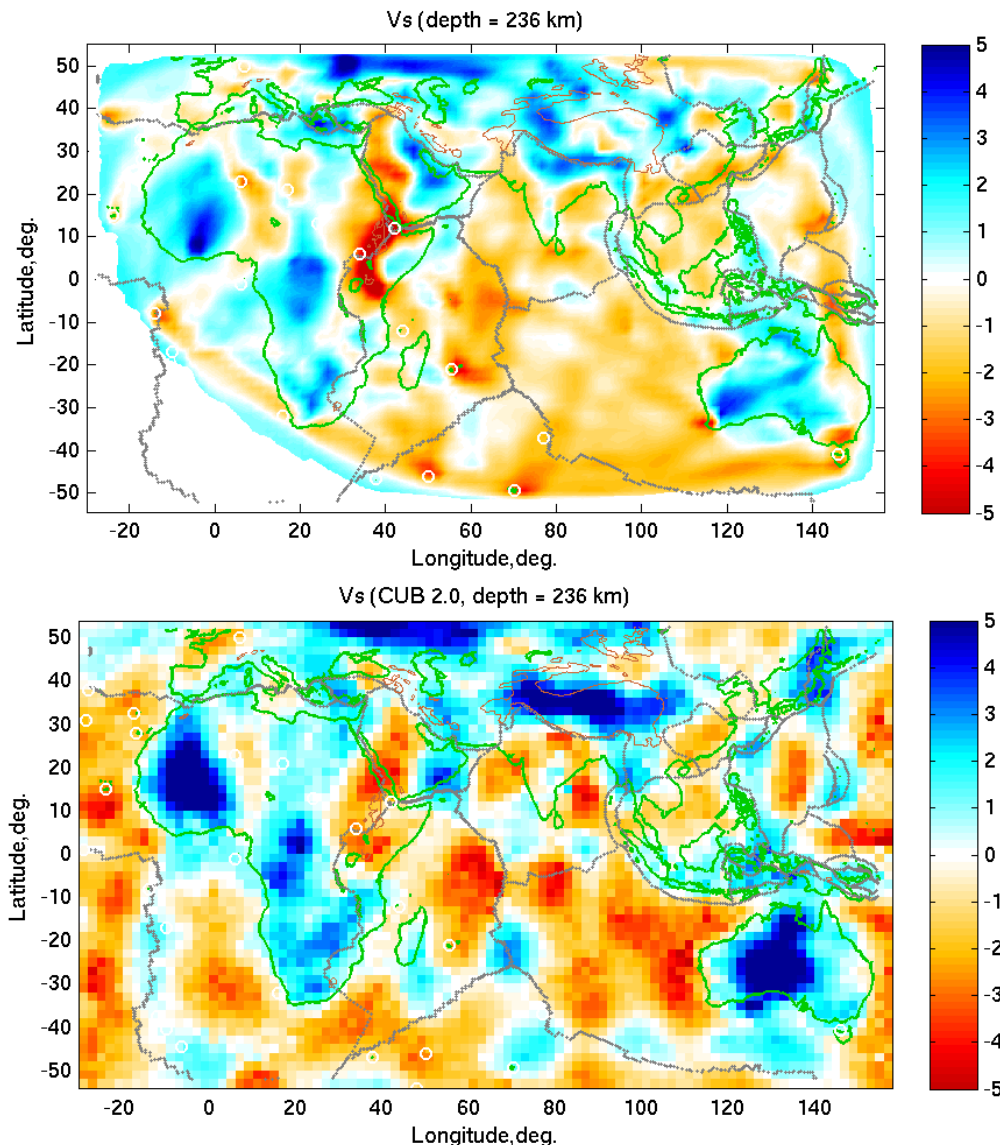


**Figure 8. (Top)** A horizontal slice of the 4<sup>th</sup>-iteration Vs model at 236 km depth from full-wave ambient noise tomography. The color scale is velocity perturbation (%) relative to the average model. The plate boundaries are shown as dotted lines. The 2000-m elevation contour (brown) approximately outlines the Tibetan plateau and other mountain ranges. **(Bottom)** The Vs velocity structure of CUB 2.0 (Ritzwoller et al., 2002) for comparison.

The above equation is discretized into inversion cells. In the first model iterations for the eastern hemisphere, we use  $2^\circ \times 2^\circ$  blocks as our inversion grids. The thickness of the blocks changes from  $\sim 14$  km near the surface to  $\sim 80$  km at  $\sim 1600$  km depth. The inversion block size may be reduced in late iterations to capture sharp velocity changes. The inverse problem is solved with LSQR (Paige and Saunders, 1982) with damping and smoothness constraints. The damping and smoothness constraints are gradually reduced until the data misfit is consistent with the estimated data uncertainty (normalized  $\chi^2 \sim 1$ ), as in Montelli et al. (2004).

Figure 8 is a comparison of the 4th-iteration Vs model from this study and that of Ritzwoller et al. (2002), which was derived from group and phase velocities of earthquake surface wave arrivals. There are notable similarities and differences between the two models. For example, the African cratons and the west Australian craton exhibit high velocity anomalies in both models. The Afar and Eastern Africa Rift are prominent low velocity anomalies in both models. One major difference between the two models is the structure beneath the Tibetan plateau, an area well sampled by ambient noise (Figure 6). CUB 2.0 has a strong high-velocity anomaly beneath the center of the plateau and low-velocity anomalies in the surrounding areas. In contrast, full-wave ambient noise tomography reveals high-velocity anomalies associated with the underthrusting Indian lithosphere in the south, the Yangtze craton in the east and the Sino-Korean craton in the north. Vs is relatively low beneath the central and northern plateau, an observation supported by regional body wave tomography (Li et al., 2008).

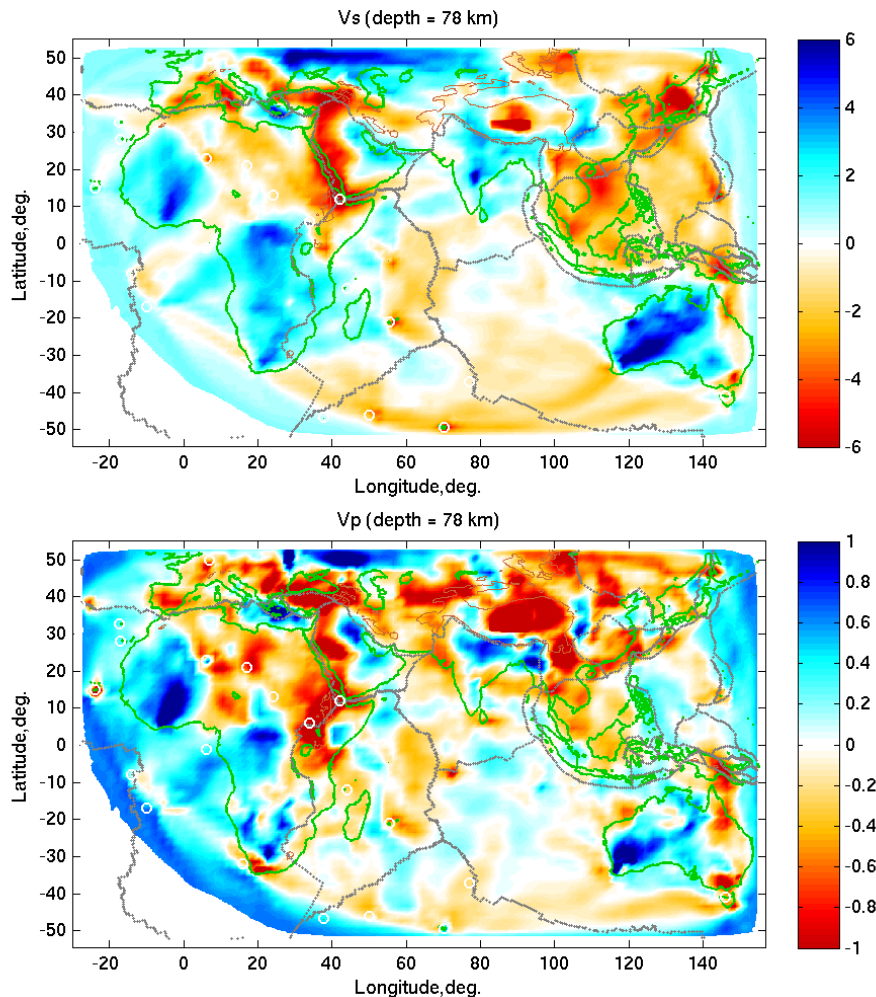


**Figure 9.** The 4<sup>th</sup>-iteration Vs (top) and Vp (bottom) velocity structures at 78 km depth. The color scales are different for Vs and Vp.

One of the reasons for the differences between the two models in Figure 8 lies in the fact that phase delays are attributed to both Vs and Vp perturbations in full-wave tomography (Figure 9). The similarity in major features

between Vs and Vp in Figure 9 suggest that Rayleigh waves yield useful resolution of the Vp structure in the crust and shallow mantle.

The very long period EGFs allow us to extend resolution through the entire upper mantle (Figure 10). The mantle transition zone beneath the Afar and East African Rift has a strong low velocity, suggesting that that rifting and hotspot volcanism have a source rooted at least in the mantle transition zone. There is a strong high-velocity anomaly immediately south of Tibet. This is interpreted as evidence for the Tethyan subducted slabs under India (Van der Voo et al., 1999). Perhaps the most intriguing result in the transition zone is the strong low velocity anomalies north of the subducted Tethyan slabs (Hafkenscheid et al., 2006). One possible explanation is that these anomalies represent elevated water content released from the subducted Tethyan slabs (Nolet and Zielhuis, 1994). van der Lee et al. (2008) observed a similar low-velocity anomaly in the upper mantle transition zone beneath the U.S. East Coast and attributed it to water released from the subducted Farallon lithosphere.

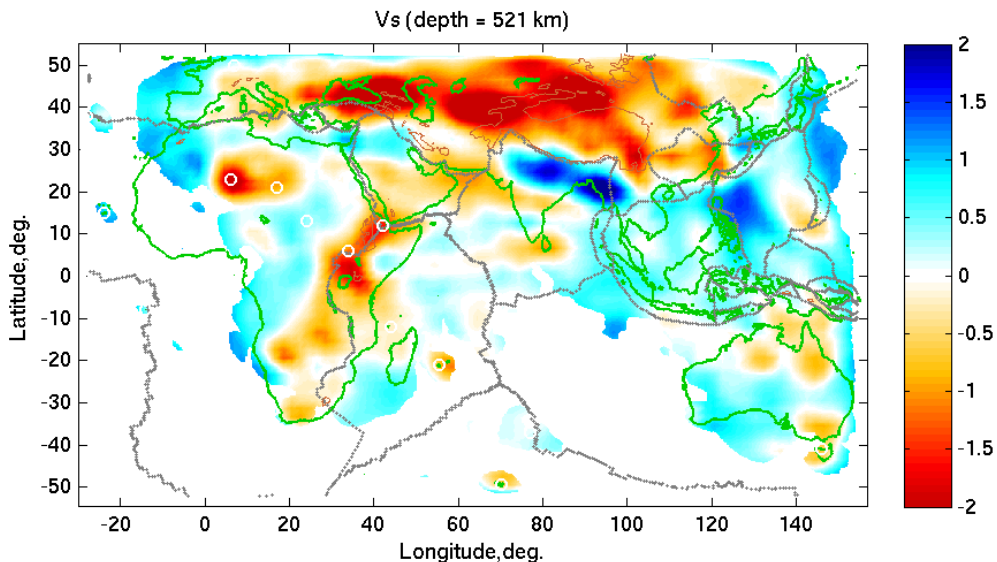


**Figure 10.** Vs structure at 521 km depth from full-wave ambient noise tomography. The color scale is velocity perturbation (%) relative to an average model.

## **CONCLUSIONS**

We collected and processed up to 21 years continuous seismic data from 184 broadband seismic stations in the eastern hemisphere (latitude 55°S-55°N; longitude 30°W-157°E). EGFs derived from ambient seismic noise show clear Rayleigh waves over a wide frequency range. We measured ~11,000 phase delays in 6 period bands ranging from 50 s to 600 s. The very long period Rayleigh waves extend Vs resolution through the entire upper mantle. The new model provides constraints on several geological processes in the region, such as the origin of the East African Rift, the extent of underthrusting of the Indian lithosphere beneath Tibet, and recycling of water by subducted slabs. Each of these geological processes warrants detailed studies that will be accomplished by the integration of ambient noise and earthquake data and the development of a hierarchical, multi-grid (resolution) model.

## **ACKNOWLEDGEMENTS**

We acknowledge the IRIS DMC for making seismic data available. Seismic Analysis Code (SAC) is used for data processing. A major part of the computation in this study was carried out on a Beowulf PC cluster purchased with a grant from the National Science Foundation (NSF OCE 0727919). Also, we thank X.F. Liang, for information regarding regional body wave tomography gleaned from personal communication.

## **REFERENCES**

Antolik, M., Y. Gu, G. Ekstrom, and A. Dziewonski (2003). J362D28: a new joint model of compressional and shear velocity in the Earth's mantle, *Geophys. J. Int.* 153: 443–466.

Antoun, T., D. Harris, T. Lay, S.C. Myers, M.E. Pasmanos, P. Richards, A.J. Rodgers, W.R. Walter, J.J. Zucca (2008). The prospect of using three-dimensional earth models to improve nuclear explosion monitoring and ground motion hazard assessment, Lawrence Livermore National Laboratory Technical Report LLNL-TR-401312.

Bassin C, G. Laske, G. Masters (2000). The current limits of resolution for surface wave tomography in North America, *Eos Trans AGU*, 81, F897.

Briggs, W.L. (1987). *A multigrid Tutorial*. Denver: University of Colorado.

Chen, P., L. Zhao, and T.H. Jordan (2007). Full 3D tomography for crustal structure of the Los Angeles Region, *Bull. Seismol. Soc. Am.* 97 (4): 1094–1120, doi: 10.1785/0120060222.

Ekström, G., G.A. Abers, S.C. Webb (2009). Determination of surface-wave phase velocities from noise and Aki's spectral formulation, *Geophys. Res. Lett.* 36, L18301, doi: 10.1029/2009GL039131.

Eisner, L. and R.W. Clayton (2001). A reciprocity method for multiple-source simulations, *Bull. Seismol. Soc. Am.* 91: 553–560.

Graves, R.W. and D.J. Wald, (2001). Resolution analysis of finite fault source inversion using one- and three-dimensional Green's functions, 1, Strong motions, *J. Geophys. Res.* 106: 8745–8766.

Hafkenscheid, E., M.J.R. Wortel, and W. Spakman (2006). Subduction history of the Tethyan region derived from seismic tomography and tectonic reconstructions, *J. Geophys. Res.* 111: B08401, doi: 10.1029/2005JB003791.

Kennett B L N, E.R. Engdahl, and R. Buland (1995). Constraints on seismic velocities in the Earth from traveltimes. *Geophys J Int.* 122: 108–124.

Li, C., Hilst, R. D. v. d., Meltzer, A. S. & Engdahl, E. R. (2008). Subduction of the Indian lithosphere beneath the Tibetan Plateau and Burma. *Earth Planet. Sc. Lett.* 274: 157–168.

Montelli, R., G. Nolet, G. Masters, F.A. Dahlen, and S.-H. Hung (2004). Global P and PP traveltimes tomography: rays versus waves, *Geophys. J. Int.* 158: 637–654.

Nishida, K., J.-P. Montagner, H. Kawakatsu (2009). Global surface wave tomography using seismic hum, *Science* 326: 112.

Nolet, G., and A. Zielhuis (1994). Low S velocities under the Tornquist-Tesisseyre zone: Evidence for water injection into the transition zone by subduction, *J. Geophys. Res.* 99 (15): 813–815, 820.

Paige, C.C. and M.A. Saunders (1982). LSQR: An algorithm for sparse linear equations and sparse least squares, *ACM Trans. Math. Software*, 8(1): 43–71.

Ritsema, J., and H.J. van Heijst (2000). Seismic imaging of structural heterogeneity in Earth's mantle: Evidence for large-scale mantle flow, *Science Progress.* 83: 243–259.

Ritzwoller, M.H., NM. Shapiro, M.P. Barmin, and A.L. Levshin (2002). Global surface wave diffraction tomography, *J. Geophys. Res.* 107, doi: 10.1029/2002JB001777.

Shen, X., H. Zhou, and H. Kawakatsu (2008). Mapping the upper mantle discontinuities beneath China with teleseismic receiver functions, *Earth Planets Space.* 60: 713–719.

Shen, Y., W. Zhang (2010). Full-wave ambient noise tomography of the northern Cascadia, SSA meeting (abstract), *Seismological Research Letters.* 81: 300.

Shen, Y., Z. Zhang, W. Zhang (2011). Moment inversions of earthquakes in the southeast Tibetan plateau using finite-difference strain Green tensor database, submitted to *Geophys. J. Int.*

Van der Lee, S., K. Regenauer-Lieb, D.A. Yuen (2008). The role of water in connecting past and future episodes of subduction, *Earth Planet. Sci. Lett.* 273: 15–27.

Van der Voo, R., W. Spakman, H. Bijwaard (1999). Tethyan subducted slabs under India, *Earth Planet. Sci. Lett.* 171: 7–20.

Zhang, W., and Y. Shen (2010). Unsplit complex frequency shifted PML implementation using auxiliary differential equation for seismic wave modeling, *Geophys.* 75 (4): 141–154.

Zhang, W., Y. Shen, L. Zhao (2011). 3D seismic wave modeling in spherical coordinate by a non-staggered finite difference method, manuscript submitted to *Geophys. J. Int.*

Zhang, Z., Y. Shen (2008). Cross-dependence of finite-frequency compressional waveforms to shear seismic wave-speeds, *Geophys. J. Int.* 174: 941–948, doi: 10.1111/j.1365-246X.2008.03840.x.

Zhang, Z., Y. Shen, and L. Zhao (2007). Finite-frequency sensitivity kernels for head waves, *Geophys. J. Int.* 171: 847–856.

Zhao, L., T.H. Jordan, K.B. Olsen, and P. Chen (2005). Fréchet kernels for imaging regional earth structure based on three-dimensional reference models, *Bull. Seismol. Soc. Am.* 95: 2066–2080.

Zhao, L., P. Chen, and T.H. Jordan (2006). Strain Green tensor, reciprocity, and their applications to seismic source and structure studies, *Bull. Seismol. Soc. Am.* 96: 1753–1763, doi: 10.1785/0120050253.

## DISTRIBUTION LIST

DTIC/OCP  
8725 John J. Kingman Rd, Suite 0944  
Ft Belvoir, VA 22060-6218 1 cy

AFRL/RVIL  
Kirtland AFB, NM 87117-5776 2 cys

Official Record Copy  
AFRL/RVBYE/Robert Raistrick 1 cy

This page intentionally left blank.